OPEN ACCESS
Journal of Innovative Optical Health Sciences
Vol. 16, No. 5 (2023) 2241003 (12 pages)

DOI: 10.1142/S1793545822410036

World Scientific
www.worldscientific.com

Discrimination and quantification of scar tissue by Mueller matrix imaging with machine learning

Xi Liu*, Yanan Sun†, Weixi Gu‡, Jianguo Sun§, Yi Wang†,¶ and Li Li*,‖

*Department of Ophthalmology, Beijing Children's Hospital
Capital Medical University, National Center for Children's Health
Beijing 100045, P. R. China

†Experimental Research Center
China Academy of Chinese Medical Sciences
Beijing 100700, P. R. China

‡China Academy of Industrial Internet
Beijing 100102, P. R. China

§Department of Ophthalmology & Visual Science
Eye & ENT Hospital, Shanghai Medical College
Fudan University, Shanghai 200031, P. R. China
¶wangyi02@tsinghua.org.cn
‖liliyk1@163.com

Received 16 June 2022
Accepted 18 August 2022
Published 3 October 2022

Scarring is one of the biggest areas of unmet need in the long-term success of glaucoma filtration surgery. Quantitative evaluation of the scar tissue and the post-operative structure with micron scale resolution facilitates development of anti-fibrosis techniques. However, the distinguishment of conjunctiva, sclera and the scar tissue in the surgical area still relies on pathologists' experience. Since polarized light imaging is sensitive to anisotropic properties of the media, it is ideal for discrimination of scar in the subconjunctival and episcleral area by characterizing small differences between proportion, organization and the orientation of the fibers. In this paper, we defined the conjunctiva, sclera, and the scar tissue as three target tissues after glaucoma filtration surgery and obtained their polarization characteristics from the tissue sections by a Mueller matrix microscope. Discrimination score based on parameters derived from Mueller matrix and machine learning was calculated and tested as a diagnostic index. As a result, the discrimination score of three target tissues showed significant difference between each other ($p < 0.001$). The visualization of the discrimination results showed significant contrast between target tissues. This study proved that Mueller matrix imaging is effective in ocular scar discrimination and paves the way

¶,‖Corresponding authors.

for its application on other forms of ocular fibrosis as a substitute or supplementary for clinical practice.

Keywords: Tissue discrimination; glaucoma filtration surgery; polarized light; Mueller matrix; machine learning.

1. Introduction

Excessive ocular fibrosis features in many significant visual impairment and is responsible for many treatment failure.[1] It happens in disease (e.g., diabetic retinopathy, macular degeneration and proliferative vitreoretinopathy), injury (e.g., corneal and conjunctival scarring after trauma or burn), surgery (e.g., scar after glaucoma filtration surgery (GFS), capsular opacification after cataract surgery, scarring around the extraocular muscles after strabismus surgery), or regenerative therapies (e.g., cellular transplantation).[2] Collectively, ocular fibrosis is one of the biggest areas of unmet need in ophthalmology. Visualization and quantification of ocular fibrosis with micrometer-scale resolution facilitates research on effective anti-scarring therapies which could potentially revolutionize the management of many diseases like glaucoma worldwide. This paper aims to provide a way of discrimination and quantification of scar tissue after GFS and paves the way for its application on other forms of ocular fibrosis.

Glaucoma is the first reason that leads to irreversible blindness in millions of people worldwide.[3,4] GFS including trabeculectomy and/or glaucoma drainage device (GDD) implantation, is warranted if topical medications cannot control the intraocular pressure (IOP).[5] By creating a channel between the anterior chamber and the subconjunctival space, the aqueous humor is drained into the bleb and absorbed by the vasculature, thus lower the IOP. Unfortunately, in a significant percentage of cases as previous studies reported, when excessive scar forms in the bleb and blocks the filtration channel, it will result in the increase of IOP and ultimate failure of the surgery.[6]

Studies ranging from new therapeutic agents targeting different pathways of wound healing processes to novel drug delivery system, and from more precise usage of anti-fibrosis medicine to improvement of surgical skills have been emerging during the past two decades.[7–9] Many imaging techniques have been deployed for measuring and/or visualizing the fibrosis tissue and determining which therapy is likely to be worthwhile. Optical coherence tomography (OCT) works well *in vivo*, however, the segmentation based on structural information of fibrosis tissues is difficult, since the scattering properties are not distinctive enough for discrimination, and the limitation in resolution has further precluded the application in microstructure observation.[10,11] Staining methods such as H&E stain, Masson trichrome stain, Van Gieson stain can assist to investigate the structure of collagen fibers in scar and yield qualitative information on collagen alignment and deposition by histopathological examination,[12] but none of them can directly outline the region of the scar.[13,14] To segment clearly the scar area, the judgement by well-trained pathologist is urgently required, however, the results may vary by their discrepancy in knowledge and experience.

Polarization imaging has shown great potential in characterizing the specific microstructural features of complex biomedical samples, especially the anisotropic fibrous components.[15] Studies have found both birefringence and depolarization in various ocular tissues. For example, birefringence in corneal stroma, the sclera, ocular muscles and tendons, trabecular meshwork, the retinal nerve fiber layer, and the scar tissue; and depolarization in melanin containing tissue like the retinal pigment epithelium, also in accumulations of pigment loaded macrophage.[16] Scar tissue can be regarded as the product of collagen fiber synthesis and the disarrangement of its density and orientation, mixed with the extracellular matrix as fiber-reinforced anisotropic soft tissue, hence polarization imaging has its distinctive advantage to visualize and analyze the scar tissue. Jan *et al.* used the polarized light microscopy (PLM) to study the collagen architecture of the eye and demonstrated that PLM can provide objective and robust data on fiber orientation with micrometer-scale resolution over a broad field of view without requiring tissue dehydration, labeling or staining.[17] Woessner *et al.* utilized a quantitative polarized light imaging system

for observing wound sections in mouse model, and thus demonstrated the increase in fiber density and thickness in the wound healing process.[18] Miyazawa *et al.* developed a tissue discrimination algorithm in anterior eye using three optical parameters obtained by polarization sensitive optical coherence tomography (PS-OCT).[10]

To develop specific parameters that can discriminate scar tissue surrounding the bleb, we adopted Mueller matrix (MM) imaging. MM is a complete description of the polarization characteristics of complex biological specimens, which contains abundant micro-structural information and optical properties.[19] It is in the form of 4×4 matrix, and contains 16 elements. However, the individual elements often lack clear physical meanings and explicit connections to specific microstructures. Recently, many studies have proposed multiple sets of polarization parameters based on physical theory, named as polarimetry basis parameters (PBPs).[20] They are functions of MM elements, and have relatively clear physical meanings. Assisted by high dimensional data processing methods, such as machine learning, several studies have shown the potential capability of PBP as diagnostic index to quantitatively evaluate distinctive pathological features. Ahmed *et al.* fed four polarization properties spectra, including depolarization (ΔT and ΔL) and retardance (RT and δ), into the machine learning classifier to distinguish the normal and adenocarcinoma colon samples.[21] Wang *et al.* applied the logistic regression models based on machine learning to determine optimal polarization parameters for the classification of lung cancer cells.[22] Dong *et al.* used the LDA-based training method to find the most efficient parameters from PBPs for the combination of new parameters which could describe the specific microstructural features of typical breast tissue diseases.[23]

In this work, we built the animal model of GDD implantation surgery and imaged the tissue section of the filtering bleb by both ordinary light microscope and MM microscope. We defined conjunctiva, sclera and scar tissue as three target tissues in the discrimination algorithm. Their polarization characteristics demonstrated in the form of MM element and PBPs at pixel level were analyzed quantitatively and were used as features of training model respectively. Analysis of variance (ANOVA) was adopted for principal feature selection and Gaussian-kernel based support vector machine (SVM) was leveraged for tissue discrimination. Each pixel of the target tissue would have a discrimination score and thus decided its classification. The performance between using MM elements and PBPs as features in the algorithm was compared. The capability of discrimination score as a diagnosis index was statistically analyzed. To our best knowledge, it is the first study on ocular scar tissue recognition based on MM imaging and its application on the model of GFS can be a paradigm for other ocular fibrosis tissues.

2. Materials and Methods

2.1. *Animal model of GFS*

In this study, six mature male New Zealand rabbits (mean body weight 1.5 kg) were used in the GFS model. The tested novel drug delivery system is the GDD coated with cyclosporine A (CsA) and poly(lactic-co-glycolic acid) (PLGA) (CsA@PLGA@GDD) which can continuously release CsA to prevent postoperative fibrosis following GFS. Details of the preparation of CsA@PLGA@GDD were described in previous work.[24] Before surgery, the rabbits were housed in the animal experiment center in EENT Hospital (Fudan University) for no less than 3 days to familiarize them with the environment. The customized CsA@PLGA GDD was implanted into each rabbit's eye. The GDD implantation surgeries were performed following the procedure described previously by one experienced ophthalmologist.[24] Figure 1(a) shows a schematic diagram of the GDD and its location after subconjunctival implantation. After 12 weeks follow-up observation, all rabbits were sacrificed by injecting air into the auricular veins. All experimental protocols, including the experiments, transportation, and care of the animals, complied with the Association for Research in Vision and Ophthalmology Statement for the Use of Animals in Ophthalmic and Vision Research and the guidelines of the Animal Care and Use Committee of Fudan University (Shanghai, China).

2.2. *Histological study of the filtering bleb*

The eyeballs of six rabbits from CsA group and control group were removed and fixed with 4% PFA for histological examination, respectively. Tissues in

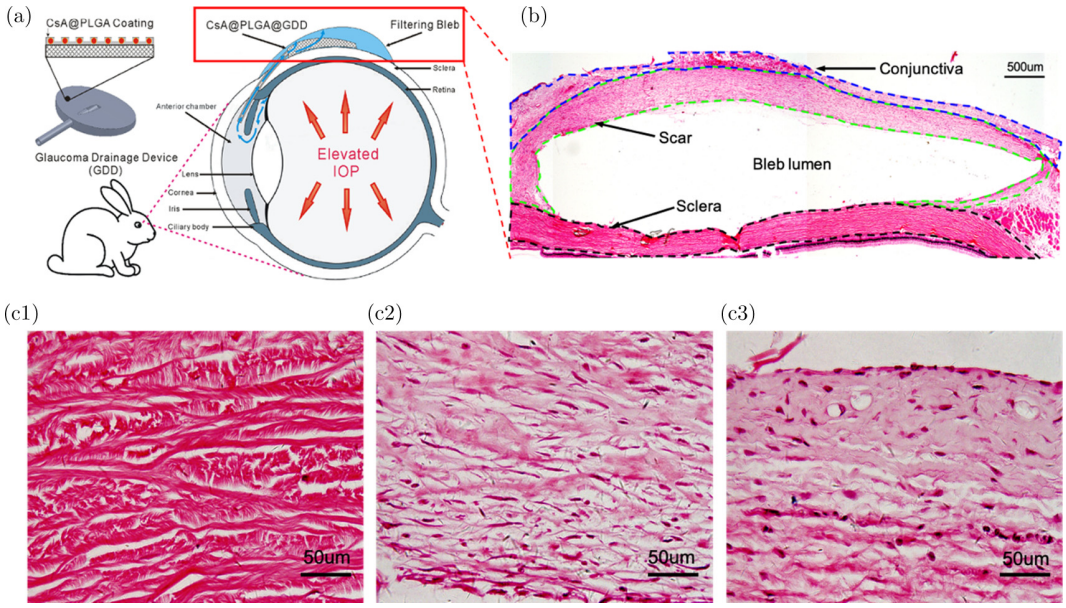

Fig. 1. Illustration of the animal model and histological study of the surgical area. (a) Schematic diagram of the animal model of GFS. Reproduced with permission from Ref. 24. (b) Image of one typical surgical field on H&E stained tissue section obtained by ordinary optical microscope (merged by 3 ROIs). Blue dashed line outline conjunctiva; green dashed line outline scar; black dashed line outline sclera. (c) Observation of three target tissues under objective lenses of 20×: (c1) sclera; (c2) scar; (c3) conjunctiva.

the surgical field including filtering bleb, the GDD/CsA@PLGA GDD inside the bleb, and the eyeball wall under GDD of each eye were trimmed from the fixed eyeball. Then the tissues were embedded in paraffin, sectioned into 10-μm-thick slides, and stained with H&E. Tissue sections were observed under the transmission microscope (Yuexian, L2050, Guangzhou, China), and the imaging data were collected by an 8-bit CCD (Jinghang, JHSM300f, Shenzhen, China). To show the entire filtering bleb in the surgical field, images of regions-of-interest (ROIs) were collected under objective lenses of 4×. Each filtering bleb is merged by three ROIs. The size of all the ROIs in this study is 1000×1000 in pixels.

2.3. *Experimental setup and PBPs*

MM microscopic imaging was obtained for the same 18 ROIs of six samples, respectively, after histological observation. The MM microscope used in this study was developed by a collaborator shown in Fig. 2(a).[25] The microscope was constructed by adding polarization state generator (PSG) and polarization state analyzer (PSA) modules into the existing optical path of the commercial transmission microscope (Liss Optical Instrument Factory, China) to facilitate fast and high precision acquisition of MM images. The PSG includes a fixed linear polarizer P1 and a rotatable quarter-wave plate R1 which is controlled by a motor (PRM1/MZ8, Thorlabs Company, USA). The PSA and 2D image detection module consists of a 50:50 non-polarized beam splitter prism and two paired division-of-focal-plane (DoFP) polarimeters (PHX050S-PC, Lucid Vision Labs Company, 16-bit, Canada), called DoFP-CCD1 and DoFP-CCD2, both with resolution of 2048×2448 pixels. The two DoFP polarimeters are fixed at the transmission end and the reflection end of the beam splitter prism. The illumination light comes from a LED at 633 nm and bandwidth $\Delta\lambda = 20$ nm. A polarization image of the sample is taken by DoFP-CCD1 through a fixed-angle phase retarder R2, and another paired image is taken directly by DoFP-CCD2. MM images are then calculated from the two paired and co-registered images.[22] To show the polarization properties of the sample clearly, all the MM elements in our results were normalized by m11. Before measuring the biological samples, MM of air (without any sample) is taken and a calibration process is carried on to obtain an approximate unit matrix with the maximum errors for both the diagonal and off-diagonal elements less than 0.005. The microscope takes an MM image in less than 10 s (Fig. 2(b)). For improving the visual effect, MM is

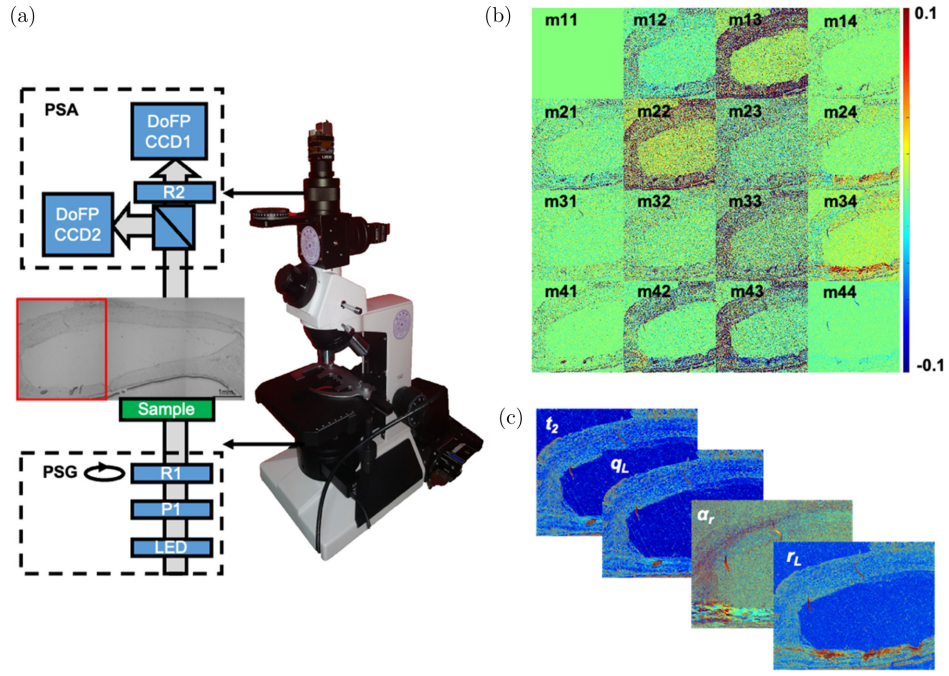

Fig. 2. (a) Photograph and schematic structure of MMM-DoFP. P: polarizer; R: quarter-wave plate. Reproduced with permission from Ref. 25. Sample shows the light intensity image of the surgical field of one typical tissue section. Rectangle box shows one ROI. (b) MM-I image of the ROI indicated in (a). The identity matrix was subtracted from the MM only for display. (c) Selected PBP images of the ROI indicated in (a).

subtracted by unit matrix I to reduce contrast differences between diagonal and off-diagonal elements. The MM-I image is shown in Fig. 2(b).

Besides using individual MM elements, this study also adopted PBPs to analyze the polarization characteristics of the target tissues. Based on our collaborators' work, altogether 104 PBPs derived from MM representing different physical meanings were summarized. This study traversed the 104 PBPs and selected the most sensitive PBPs which could show difference between target tissues both via contrast on the image and the following principal feature selection algorithm.

2.4. *Tissue discrimination via principal feature selection and Gaussian-Kernel SVM*

2.4.1. *Dataset*

To distinguish scar tissue from the surgical field, three main types of tissues surrounding the bleb (i.e., sclera, conjunctiva and the scar tissue) have been set as the target tissues. Training and testing were completed in 18 ROIs (3 ROIs per tissue section for each eye). 9 ROIs from 3 eyes were used for training, the other 9 ROIs from 3 eyes were used for testing. In order to improve the signal-to-noise ratio of the image, we used Gaussian filter to preprocess the images. Regions that can be considered as a part of a target tissue is labeled manually on the MM image data. Labeling of the target tissues was based on the anatomical and histological features of the tissues assisted with the corresponding light microscopic imaging. Pixels in the labeled regions from all the 18 ROIs were collected and formed the datasets for discrimination. The machine learning classifier randomly sampled 300,000 pixels from each target tissue for training and testing. Each pixel has two sets of polarization features, i.e., 16 MM elements and 104 PBPs. The performance of using different sets of features were compared and the principal features for discrimination were selected.

2.4.2. *Principal feature selection via ANOVA*

Analysis of variance (ANOVA) F-test was adopted to compare the importance of the features in distinguishing target tissues. The methods based on F-test estimate the degree of linear dependency between two random variables. We calculated the target pixels with 16 MM elements features and 104

PBPs features, respectively, by ANOVA, and got the ranking of these features' importance ratio. The values of the top 10 importance ratio were normalized by the top one feature (MM element or PBP). To analyze data distribution of three target tissues on different polarization parameters, their mean value and standard deviation of MM elements and the PBPs ranking top 10 was plotted respectively.

2.4.3. *Discrimination of target tissues via Gaussian-kernel SVM*

Based on empirical experiments, most of the polarization features conform to approximate Gaussian distributions. Invoked by this prior knowledge, we adopted Gaussian kernel in the SVM classifier for the discrimination of the three target tissues.[26,27] Give consideration to the working efficiency and classification effect of the classifier, we used PBPs ranking top 30 based on principle feature selection for discrimination and compared its performance with using 16 MM elements as features. SVM returned three discrimination scores on each pixel, predicting the probability of the pixel belongs to each target tissue classification. The maximum score was used for the pixel assignment. Logloss, accuracy, precision, recall and area under ROC curve (AUC) were calculated by feeding the testing data and the target tissues ground truth into the trained model to predict and evaluate each pixel in the testing sample.

2.4.4. *Display of the discrimination results*

For display of the discrimination results, all the pixels on the sample images were calculated based on the model obtained from training. Specific pseudo-colors corresponding to each tissue classification result were attributed to every pixel in the image: red indicates sclera, blue indicates conjunctiva, and green indicates scar tissue. The color bar was set according to the range of the discrimination score, the higher the discrimination score is, the darker the corresponding color. Regions without tissue on the slide were taken as background, and were automated, segmented and masked by connected components labeling (CCL) algorithm[30,31] (Matlab, version R2016a; MathWorks, Inc., MA, USA). Black in the discrimination results corresponds to pixels that were masked as background.

2.5. *Clinical statistical analysis of the discrimination score*

To evaluate the efficacy of the discrimination score as a diagnosis index, one-way ANOVA was performed to compare the obtained scar tissue discrimination score among sclera, conjunctiva and scar tissue. The differences were considered statistically significant if $p < 0.05$. The statistical analyses were carried out using statistical software (SPSS, version 19.0; IBM Corp., Armonk, NY, USA).

3. Results and Discussion

3.1. *Histological features of the target tissues*

The histological morphology of the 18 ROIs in 6 glaucoma post-operative ocular tissue samples were studied by ordinary optical microscope first. Figure 1 illustrates the animal surgery model and histological features obtained by ordinary optical microscope. Figure 1(a) is the schematic diagram showing the appearance of the customized CsA@PLGA GDD, and the location of the GDD after surgery. Blue arrows show the direction of aqueous humor flowing through the CsA@PLGA GDD tube after GFS. The rectangular box on the eyeball diagram shows the place for tissue sectioning after trimming. Figure 1(b) is the image of the H&E stained tissue section obtained by ordinary optical microscope. It is merged by 3 ROIs under objective lenses of 4×. Since the cross-sectioned silicon GDD body and tube could not be sticked to the slide, the inside of bleb shown on the slide was an empty lumen. The regions of three target tissues can be vaguely distinguished only by H&E staining, and are outlined by dashed lines in different color based on anatomical position and clinician's experience. Figure 1(c) shows detailed histological features of target tissues at high magnification. We can figure out that sclera stroma (Fig. 1(c1)) has its typical hierarchical structure of the type I collagen-rich scleral extracellular matrix and is devoid of vessels.[28] Conjunctiva (Fig. 1(c3)) has much looser arrangement of the fiber and is highly vascularized compared with sclera. Scar tissue (Fig. 1(c2)) which is anatomically close to conjunctiva and sclera after GFS, is mainly composed of irregularly arrangement of type VIII and type I collagens and lots of fibroblasts among the fibers.

Although there are many studies on evaluation of the filtering blebs after glaucoma surgery based on morphology and functionality,[29,30] there are few works focusing on the quantitative evaluation of the scar tissues directly. In previous study on the anti-fibrosis efficiency of the CsA@PLGA GDD, we met the problem of the quantitative evaluation of the scar area between the control group and the new material group. As a substitute, we could only give a qualitative comparation based on pathologists' experience. This also happened in lots of basic research on anti-fibrosis techniques. Clinicians have to define the scar based on description of the irregular morphology.[31] One of the main reasons can be considered as that both the conjunctiva and the sclera surrounding the scar tissue in the surgical area are formed by connective tissue, which means, their main components are similar with scar. Connective tissues consist three main components: fibers (elastic and collagenous fibers), ground substance and cells.[32] Scar tissue is formed by enhanced fibroblast proliferation, synthesis and secretion of collagen, and deposition of extracellular matrix.[33] The differences among these three connective tissues are the proportion, organization and the orientation of the main components. For these aspects, MM microscope imaging can provide much more relevant information than ordinary light microscopy based on traditional staining. The results of histological study confirmed us with further study on target tissue by MM microscope imaging.

3.2. *Polarization properties of the surgical field obtained by MMM-DoFP*

The corresponding polarization properties of the 18 ROIs in 6 glaucoma post-operative ocular tissue samples examined were obtained by MMM-DoFP. Figure 2(a) shows the photograph and schematic structure of MMM-DoFP. Diagram of sample shows the light intensity image of the surgical field of one typical tissue section obtained by MMM-DoFP. Inside the rectangle box, is one ROI. We can figure out that only by light intensity the H&E staining shows few information of the differences among target tissues. Figure 2(b) presents the calculated MM-I images of the ROI indicated in Fig. 2(a). It can be observed that different MM element shows different power to distinguish target tissues. The nine elements in the upper left corner of the matrix show less difference while m24, m42, m34 and m43 show more obvious difference. Differences on these four elements indicate that the anisotropy of tissue is mainly contributed by birefringence of the fiber but not scattering.[34] Besides, birefringence of the sclera looks more significant than other tissues. In order to verify the result indicated by MM elements and find parameters with more explicit physical meaning to distinguish the target tissues, we traversed 104 images calculated by PBPs on each ROI, and evaluated their power to show target tissues by comparing the contrast on the images. Figure 2(c) presents selected images calculated by PBPs with sharp contrast of the ROI indicated in Fig. 2(a). Their corresponding physical meanings are anisotropy degree (t_2) derived from MM transformation (MMT)[35]; capability of transforming between linear and circular polarizations (q_L and r_L) and orientation of fast axis (α_r) which belong to rotation invariant parameters.[36] Compared with the contrast shown in MM element images, PBP images revealed more obvious difference between the target tissues, and confirmed us with its potential in the discrimination method.

Although MM microscopic imaging revealed much more microstructure information of the target tissues than ordinary light microscopic imaging did, only by using either MM element images or PBP images, the contrast between target tissues is not significant enough. Also, to traverse 104 PBPs is time consuming and inefficient. More specific features need to be extracted from the polarization properties. Thus, we leveraged the principal feature selection to analyze the polarization characteristics of the target tissues quantitatively and to find the decisive features in discrimination.

3.3. *Principal feature selection of MM elements and PBPs*

Feature reduction based on ANOVA is often used to enhance the generalization of model and thus increase the inference performance. Figures 3(a) and 4(a) show the ranking of top 10 important features of MM elements and PBPs in discriminating target tissues based on ANOVA respectively. Here, the importance ratios of the features are normalized by the top 1 feature and presented in the descending order. Figures 3(b) and 4(b) demonstrate the distribution of the three target tissues'

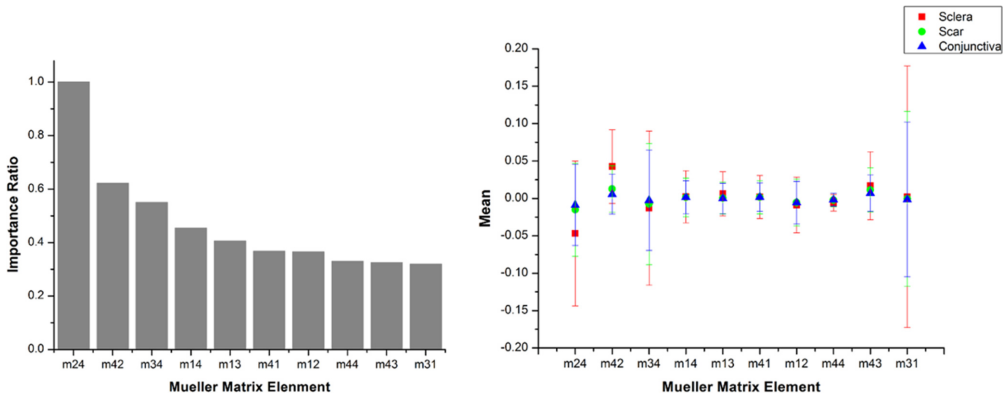

(a) (b)

Fig. 3. (a) Principal feature selection for MM elements based on ANOVA. Histogram shows the importance ratio of the MM elements ranking top 10 in discriminating the target tissues. (b) Distribution of the corresponding MM element values (mean and standard deviation) of the three target tissues. The figure indicates that simply using one feature or linear combination of the features may not be sufficient in the discrimination methods.

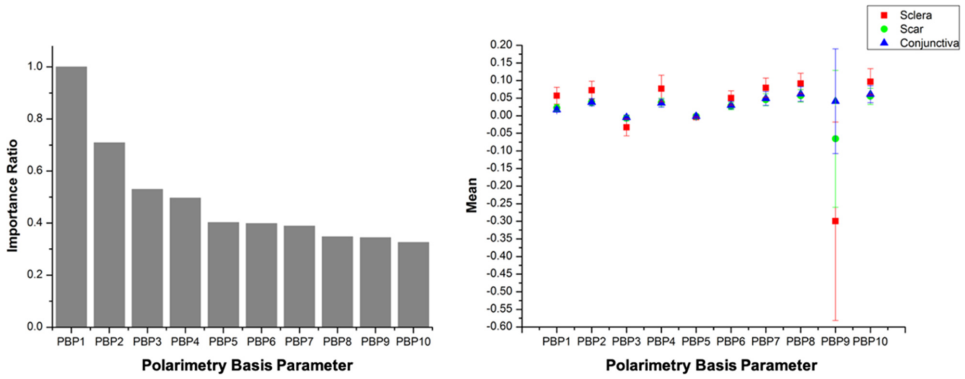

(a) (b)

Fig. 4. (a) Principal feature selection for PBPs based on ANOVA. Histogram shows the importance ratio of the PBPs ranking top 10 in discriminating the target tissues. (b) Distribution of the corresponding PBP's value (mean and standard deviation) of three target tissues. The figure indicates that simply using one feature or linear combination of the features may not be sufficient in the discrimination methods.

pixel values in MM element and PBP images after the principal feature selection. The mean and standard deviation of the randomly sampled pixels from each target tissue in the training dataset are compared and analyzed.

We can figure out from Fig. 3(a) that the most important two MM elements in the discrimination are m24 and m42. In addition, the mean values of the two features of the three target tissues are differentiated, whereas those of the following features are relatively concentrated, as shown in Fig. 3(b). In Fig. 4(a), PBP1 and PBP5 represent linear and circular depolarization calculated by MM logarithmic decomposition, respectively; PBP2 is diattenuation; PBP3 and PBP4 are birefringence asymmetry related parameters; PBP6 has close relationship with birefringence; PBP7 and PBP8 are depolarization and retardance proposed by MM polar decomposition respectively. In Fig. 4(b), the standard deviations of the pixel values are relatively smaller than that on MM element images. Also, it can be seen that the mean value of sclera is always significantly different from the other two target tissues on each PBP.

Compared with MM elements, the selected PBPs used as input features allows further analysis of physical meaning for the discrimination of the three types of tissues surrounding the bleb. Among the

top 10 features, the properties related with depolarization, diattenuation and birefringence make great contributions for the classification. The previous experimental studies and Monte Carlo simulations demonstrated that depolarization is closely related to the size distributions of the scatterers[37]; diattenuation is more obvious in cylindrical scatterers with small diameters[38]; birefringence could characterize the proliferative fibrous structures in biological tissues.[39] Therefore, Fig. 4 allows us to further analyze that depolarization may be caused by the accumulation of the fibroblast cells; diattenuation and birefringence may be introduced by the increase of the newly-formed thinner fibrous structures or coarse collagen bundles respectively. Also, distribution of the mean value of target tissue pixels can show some differences on the selected features to certain extent, however, the differences are not significant enough to distinguish the target tissues from each other. Hence, simply using one feature or linear combination of the features may not be sufficient in the discrimination methods. For this aspect, machine learning classifier was leveraged. In this paper, SVM was chosen based on preliminary study and its advantage that can be easily extended into a nonlinear classifier by adopting the kernel trick, which makes it enable to cope with the dataset even though it holds a high-dimensional/nonlinear distribution.

3.4. *Scar tissue discrimination*

Two sets of features, that is, top 30 MM elements and PBPs are applied to SVM classifiers for discrimination of the three target tissues respectively. Their performance was evaluated and presented in Table 1. Logloss, accuracy, precision, recall and AUC were calculated by feeding the testing data and the target tissues ground truth into the trained model to predict and evaluate each pixel in the testing sample. The results demonstrate that (i) the higher AUC for scar is 0.85, higher overall accuracy for the three target tissues is 0.74, the lower logloss is 0.58; (ii) using PBPs as features show significant better performance than using MM elements since it wins in every evaluation index. In particular in the discrimination of scar, it overcomes the performance of MM elements by more than 10% in either precision, recall or AUC. The results are consistent with our observation of data distribution in Figs. 3 and 4. Over fitting is within the acceptable range by comparing the accuracy of training data with testing data. The accuracy in the training data is 0.79 and is 0.05 higher than that in the testing data. Based on the performance, we utilized the training model by using the top 30 PBPs as features to test the sample and displayed the discrimination result in Fig. 5.

In comparison with the ordinary imaging method, the images of a typical filtering bleb tissue section obtained by ordinary optical microscope, MMM-DoFP, and the discrimination results are exhibited below. Since the illumination light comes from an LED at 633 nm and bandwidth $\Delta\lambda = 20$ nm in MMM-DoFP, H&E staining can provide almost no information with the observation of the microstructure in Fig. 5(b). Either in Figs. 5(a) or 5(b), we could not distinguish the three target tissues in a good contrast. However, in Fig. 5(c), the display of the discrimination results in pseudo-color image gives us better contrast of the target tissues. Clinicians can outline the scar area in assistant with the boundary where blue meets green. Figures 5(d)–5(f) show the results to observe the discrimination results of each target tissue separately. Although there are some wrong discrimination results, it is not a significant error in clinical practice and can be easily corrected based on the sample's anatomical structure.

Table 1. Performance of the discrimination of three target tissues based on MM element versus PBP.

	Sclera		Scar		Conjunctiva		3 target tissues	
	MM element	PBP	MM element	PBP	MM element	PBP	MM element	PBP
Precision	0.80	0.96	0.54	0.68	0.58	0.59		
Recall	0.79	0.84	0.50	0.61	0.65	0.76		
AUC	0.91	0.96	0.76	0.85	0.84	0.86		
Accuracy							0.67	0.74
Logloss							0.73	0.58

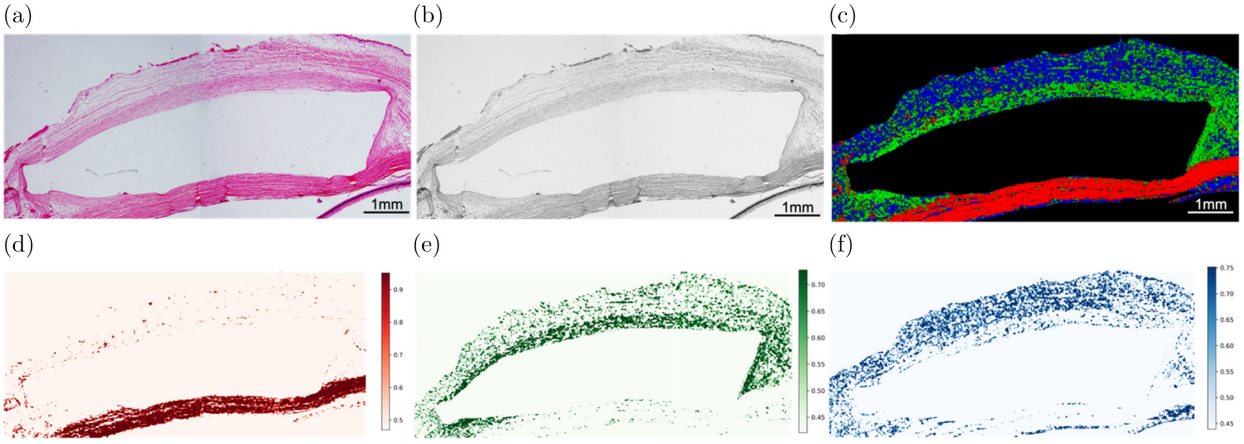

Fig. 5. Comparison of different imaging methods for a typical filtering bleb (merged by 3 ROIs) after GFS. (a) Image obtained by ordinary optical microscope based on H&E stained tissue section. (b) Light intensity image obtained by MMM-DoFP based on H&E stained tissue section. (c) Image of discrimination results based on PBPs and machine learning. (d)–(f) Display of the discriminated 3 target tissues respectively. From (c)–(f), discriminated sclera (red pixel); discriminated scar (green pixel); discriminated conjunctiva (blue pixel). Color bar is set based on the discrimination score.

To summarize the results, this discrimination method based on MM imaging and machine learning has several advantages over conventional method. (i) The discrimination method gives a more objective and concrete results of the ocular fibrosis tissue. Previously, evaluation of the scar tissue after GFS based on histological morphology can only rely on semi-quantitative scoring system incorporated visual reference standards. For example, to compare the tested sample with the controlled sample and give a grade on a scale of 0–4: 0, same as control eye; 1, 1–25% of control; 2, 26–50% of control; 3, 51–75% of control; 4, more than 75% of control.[13] By adopting the discrimination score, more studies on the relationship between discrimination score and the functionality of the blebs can be thus conducted. (ii) We note that, the discrimination is not based on structural information, but directly on the polarization properties of the tissues. So, it will not be affected by various shapes of the blebs. It visualizes the region of scar, and, hence, provides an objective measurement that can directly reflect the histopathological change during the scar formation. (iii) Since the light intensity image obtained by MMM-DoFP has rare microstructure information provided by staining, it shows the promising possibility in discrimination by nonlabeled tissue section. Overall, with the advantages of simple structure, fast imaging speed and low cost, this method exhibited the ability in discriminating the ocular scar tissue.

3.5. *Evaluation of the tissue discrimination score*

The ultimate goal in this study was to find a method for ocular scar discrimination which can be used as a substitute or supplementary for clinical practice. In consideration of this point, we tested the power of the discrimination scores which each pixel of three target tissues will be assigned from the algorithm as a diagnostic index. One-way ANOVA was used for statistical analysis, and the results showed significant difference between the discrimination score of each target tissues ($p < 0.001$). This result further confirmed the capability of the discrimination score as an efficient parameter to assist ocular scar tissue discrimination in glaucoma post-operative tissue samples.

This study takes pixels as samples for the training dataset, the number of individuals providing the pixels is still small. A larger sample size is essential to further qualify the discrimination algorithm. Since the analyzed data already fitted the Gaussian distributions, the algorithm is still suitable for a larger sample size.

4. Conclusion

In conclusion, we realized the discrimination of not only the scar tissue but also the conjunctiva and the sclera surrounding the scar based on MM microscopy combined with machine learning algorithm.

Also, the virtual staining displaying the three target tissues based on the discrimination score showed better contrast than conventional staining methods. The discrimination score is helpful as a diagnostic index in ophthalmological pathology. This study showed tremendous potential of applying MM microscopy on ocular fibrosis tissue, especially the outer sphere wall of the eyeball, which can help the understanding in pathophysiology of aging and refractive problem such as myopia.

Conflict of Interest

The authors declare no conflict of interest.

Acknowledgments

This work was supported by the Natural Science Foundation of Beijing (No. 7194266); Beijing Municipal Administration of Hospitals' Youth Program (No. QML20191206); Fundamental Research Funds for the Central Public Welfare Research Institutes (No. XTCX2021002); and Scientific and technological innovation project of China Academy of Chinese Medical Sciences (No. CI2021A00601).

References

1. F. Mallone, R. Costi, M. Marenco, R. Plateroti, A. Minni, G. Attanasio, M. Artico, A. Lambiase, "Understanding drivers of ocular fibrosis: Current and future therapeutic perspectives," *Int. J. Mol. Sci.* **22**(21), 11748 (2021).
2. P. T. Khaw, Y. Bouremel, S. Brocchini, C. Henein, "The control of conjunctival fibrosis as a paradigm for the prevention of ocular fibrosis-related blindness, Fibrosis has many friends," *Eye* **34**(12), 2163–2174 (2020).
3. J. Swogger, I. P. Conner, C. Happ-Smith, M. C. Kemmerer, D. R. Julian, R. Davis, A. Wells, J. S. Schuman, C. C. Yates, "Novel combination therapy reduces subconjunctival fibrosis after glaucoma filtration surgery in the rabbit model," *Clin. Exp. Ophthalmol.* **49**(1), 60–69 (2021).
4. S. Kwon, S. H. Kim, D. Khang, J. Y. Lee, "Potential therapeutic usage of nanomedicine for glaucoma treatment," *Int. J. Nanomed.* **15**, 5745–5765 (2020).
5. I. Durai, S. Pallamparthy, G. V. Puthuran, H. K. Wijesinghe, M. S. Uduman, S. R. Krishnadas, A. L. Robin, P. Palmberg, S. J. Gedde, "Outcomes of glaucoma drainage device implantation and trabeculectomy with mitomycin C in glaucoma secondary to aniridia," *Am. J. Ophthalmol.* **227**, 173–181 (2021).
6. Z. Dai, X. Yu, J. Sun, X. Sun, "Grooved glaucoma drainage devices that continuously deliver cyclosporine a decrease postsurgical scar formation in rabbit eyes," *Invest. Ophthalmol. Vis. Sci.* **58**(3), 1692–1701 (2017).
7. J. Sun, Y. Lei, Z. Dai, X. Liu, T. Huang, J. Wu, Z. P. Xu, X. Sun, "Sustained release of brimonidine from a new composite drug delivery system for treatment of glaucoma," *ACS Appl. Mater. Interfaces* **9**(9), 7990–7999 (2017).
8. C. Yu-Wai-Man, P. T. Khaw, "Developing novel anti-fibrotic therapeutics to modulate post-surgical wound healing in glaucoma: Big potential for small molecules," *Expert Review Ophthalmol.* **10**(1), 65–76 (2015).
9. B. Amoozgar, S. C. Lin, Y. Han, J. Kuo, "A role for antimetabolites in glaucoma tube surgery: Current evidence and future directions," *Curr. Opin. Ophthalmol.* **27**(2), 164–169 (2016).
10. A. Miyazawa, M. Yamanari, S. Makita, K. Miura, K. Kawana, K. Iwaya, H. Goto, Y. Yasuno, "Tissue discrimination in anterior eye using three optical parameters obtained by polarization sensitive optical coherence tomography," *Opt. Exp.* **17**(20), 17426–17440 (2009).
11. M. Kosugi, T. Kokubun, S. Tsuda, M. Yamanari, T. Nakazawa, "Usefulness of polarization-sensitive optical coherence tomography-derived attenuation-coefficient images to visualize the internal structure of the filtering bleb," *Curr. Eye. Res.* **46**(4), 606–609 (2021).
12. H. L. Zhao, C. P. Zhang, H. Zhu, Y. F. Jiang, X. B. Fu, "Autofluorescence of collagen fibres in scar," *Skin Res. Technol.* **23**(4), 588–592 (2017).
13. A. L. Mead, T. T. Wong, M. F. Cordeiro, I. K. Anderson, P. T. Khaw, "Evaluation of anti-TGF-beta2 antibody as a new postoperative anti-scarring agent in glaucoma surgery," *Invest. Ophthalmol. Vis. Sci.* **44**(8), 3394–3401 (2003).
14. T. W. Perkins, B. Faha, M. Ni, J. A. Kiland, G. L. Poulsen, D. Antelman, I. Atencio, J. Shinoda, D. Sinha, L. Brumback, "Adenovirus-mediated gene therapy using human p21WAF-1/Cip-1 to prevent wound healing in a rabbit model of glaucoma filtration surgery," *Arch. Ophthalmol. (Chicago, Ill: 1960)* **120**(7), 941–949 (2002).
15. P. Y. Lee, B. Yang, Y. Hua, S. Waxman, Z. Zhu, F. Ji, "Sigal IA: Real-time imaging of optic nerve head collagen microstructure and biomechanics using instant polarized light microscopy," *Exp. Eye Res.* **217**, 108967 (2022).
16. M. Pircher, C. K. Hitzenberger, "Schmidt-Erfurth U: Polarization sensitive optical coherence

tomography in the human eye," *Prog. Retin. Eye Res.* **30**(6), 431–451 (2011).
17. N. J. Jan, J. L. Grimm, H. Tran, K. L. Lathrop, G. Wollstein, R. A. Bilonick, H. Ishikawa, L. Kagemann, J. S. Schuman, I. A. Sigal, "Polarization microscopy for characterizing fiber orientation of ocular tissues," *Biomed. Opt. Exp.* **6**(12), 4705–4718 (2015).
18. A. E. Woessner, J. D. McGee, J. D. Jones, K. P. Quinn, "Characterizing differences in the collagen fiber organization of skin wounds using quantitative polarized light imaging," *Wound Repair Regen.* **27**(6), 711–714 (2019).
19. C. He, H. H. He, J. T. Chang, B. G. Chen, H. Ma, M. J. Booth, "Polarisation optics for biomedical and clinical applications: A review," *Light-Sci. Appl.* **10**(1), 194 (2021).
20. A. L. Hou, X. J. Wang, Y. J. Fan, W. B. Miao, Y. Dong, X. W. Tian, J. B. Zou, H. Ma, "Polarimetry feature parameter deriving from Mueller matrix imaging and auto-diagnostic significance to distinguish HSIL and CSCC," *J. Innov. Opt. Health Sci.* **15**(1), 2142008 (2022).
21. I. Ahmad, M. Ahmad, K. Khan, S. Ashraf, S. Ahmad, M. Ikram, "Ex vivo characterization of normal and adenocarcinoma colon samples by Mueller matrix polarimetry," *J. Biomed. Opt.* **20**(5), 56012 (2015).
22. Y. Wang, J. Wang, J. Meng, G. Ding, Z. Shi, R. Wang, X. Zhang, "Detection of non-small cell lung cancer cells based on microfluidic polarization microscopic image analysis," *Electrophoresis* **40**, 1202–1211 (2018).
23. Y. Dong, J. C. Wan, L. Si, Y. X. Meng, Y. M. Dong, S. X. Liu, H. H. He, H. Ma, "Deriving polarimetry feature parameters to characterize microstructural features in histological sections of breast tissues," *IEEE Trans. Bio-Med. Eng.* **68**(3), 881–892 (2021).
24. Z. Dai, X. Yu, J. Hong, X. Liu, J. Sun, X. Sun, "Development of a novel CsA-PLGA drug delivery system based on a glaucoma drainage device for the prevention of postoperative fibrosis," *Mater. Sci. Eng. C, Mater. Biol. Appl.* **66**, 206–214 (2016).
25. T. Huang, R. Meng, J. Qi, Y. Liu, X. Wang, Y. Chen, R. Liao, H. Ma, "Fast Mueller matrix microscope based on dual DoFP polarimeters," *Opt. Lett.* **46**(7), 1676–1679 (2021).
26. J. A. Suykens, J. Vandewalle, "Least squares support vector machine classifiers," *Neural Process. Lett.* **9**(3), 293–300 (1999).
27. C.-W. Hsu, C.-C. Chang, C.-J. Lin, A practical guide to support vector classification (2003).
28. C. Boote, I. A. Sigal, R. Grytz, Y. Hua, T. D. Nguyen, M. J. A. Girard, "Scleral structure and biomechanics," *Prog. Retin. Eye Res.* **74**, 100773 (2020).
29. L. B. Cantor, A. Mantravadi, D. WuDunn, K. Swamynathan, A. Cortes, "Morphologic classification of filtering blebs after glaucoma filtration surgery: The Indiana bleb appearance grading scale," *J. Glaucoma* **12**(3), 266–271 (2003).
30. K. Kawana, T. Kiuchi, Y. Yasuno, T. Oshika, "Evaluation of trabeculectomy blebs using 3-dimensional cornea and anterior segment optical coherence tomography," *Ophthalmology* **116**(5), 848–855 (2009).
31. A. P. Wells, M. F. Cordeiro, C. Bunce, P. T. Khaw, "Cystic bleb formation and related complications in limbus- versus fornix-based conjunctival flaps in pediatric and young adult trabeculectomy with mitomycin C," *Ophthalmology* **110**(11), 2192–2197 (2003).
32. J. J. Tomasek, G. Gabbiani, B. Hinz, C. Chaponnier, R. A. Brown, "Myofibroblasts and mechano-regulation of connective tissue remodelling," *Nat. Rev. Mol. Cell Biol.* **3**(5), 349 (2002).
33. O. Yamanaka, A. Kitano-Izutani, K. Tomoyose, P. S. Reinach, "Pathobiology of wound healing after glaucoma filtration surgery," *BMC Ophthalmol.* **15**, 157 (2015).
34. H. H. He, M. H. Sun, N. Zeng, E. Du, S. X. Liu, Y. H. Guo, J. Wu, Y. H. He, H. Ma, "Mapping local orientation of aligned fibrous scatterers for cancerous tissues using backscattering Mueller matrix imaging," *J. Biomed. Opt.* **19**(10), 106007 (2014).
35. H. H. He, R. Liao, N. Zeng, P. C. Li, Z. H. Chen, X. Liu, H. Ma, "Mueller matrix polarimetry-an emerging new tool for characterizing the microstructural feature of complex biological specimen," *J. Lightwave Technol.* **37**(11), 2534–2548 (2019).
36. P. C. Li, D. H. Lv, H. H. He, H. Ma, "Separating azimuthal orientation dependence in polarization measurements of anisotropic media," *Opt. Exp.* **26**(4), 3791–3800 (2018).
37. H. H. He, N. Zeng, D. Z. Li, R. Liao, H. Ma, "Quantitative Mueller matrix polarimetry techniques for biological tissues," *J. Innov. Opt. Health Sci.* **5**(3), 1250017 (2012).
38. C. H. Shao, B. G. Chen, H. H. He, C. He, Y. X. Shen, H. Y. Zhai, H. Ma, "Analyzing the influence of imaging resolution on polarization properties of scattering media obtained from Mueller matrix," *Front. Chem.* **10**, 936255 (2022).
39. Y. Dong, J. Qi, H. H. He, C. He, S. X. Liu, J. Wu, D. S. Elson, H. Ma, "Quantitatively characterizing the microstructural features of breast ductal carcinoma tissues in different progression stages by Mueller matrix microscope," *Biomed. Opt. Exp.* **8**(8), 3643–3655 (2017).